UNIVERSITÀ DEGLI STUDI DI PADOVA

Dipartimento di Fisica e Astronomia "Galileo Galilei"

Corso di Laurea in Fisica

Tesi di Laurea

Analisi della distribuzione di cesio in una sorgente di ioni negativi, per mezzo di una diagnostica spettroscopica di assorbimento.

Analysis of caesium distribution in a negative ion source by means of absorption spectroscopy diagnostics.

Relatore

Prof. Gianluigi Serianni

Correlatore

Dr. Marco Barbisan

Laureando

Luca Baldini 1187541

Anno Accademico 2022/2023

Sommario

La fusione nucleare è tra i più ambiziosi progetti di produzione di energia a basso impatto ambientale del futuro. Attualmente a Cadarache, nel sud della Francia, è in costruzione il più grande esperimento al mondo sulla fusione termonucleare controllata: ITER. Al fine di raggiungere le prestazioni ideali per ottenere la fusione nucleare all'interno di ITER è necessario adottare sistemi di riscaldamento addizionali. Tra i metodi più importanti rientra l'iniezione di fasci di particelle neutre. Presso il Consorzio RFX a Padova è in corso la sperimentazione su SPIDER (Source for Production of Ion of Deuterium Extracted from RF plasma), il prototipo della sorgente di ioni negativi che verrà impiegata negli iniettori di fasci neutri. Gli ioni negativi sono funzionali alla produzione di fasci neutri, la cui corrente deve essere massimizzata al fine di portare la temperatura centrale del plasma all'interno di ITER a 10 keV–15 keV.

Uno tra i principali risultati che SPIDER dovrà raggiungere sarà ottenere una densità di corrente di ioni negativi estratti H^- di $355\,\mathrm{Am^{-2}}$ e di ioni D^- di $285\,\mathrm{Am^{-2}}$. Per raggiungere questi obiettivi è essenziale evaporare cesio all'interno della sorgente. Il cesio abbassa il potenziale di estrazione delle superfici aumentando così il tasso di conversione di neutri e ioni positivi in H^-/D^-; è quindi di fondamentale importanza monitorare densità e distribuzione del cesio all'interno di SPIDER. La diagnostica che si utilizza per controllare la densità e l'uniformità del cesio neutro è la Laser Absorption Spectroscopy (LAS). La tesi si concentra principalmente su quest'ultima, migliorando le stime di densità effettuate nella campagna sperimentale 2021 e approfondendo la conoscenza sulla distribuzione del cesio all'interno di SPIDER in condizioni di vuoto e di plasma.

I risultati ottenuti dalle analisi mostrano che il cesio è distribuito principalmente nella parte medio alta della sorgente e la sua presenza è fortemente dipendente dall'evaporazione dei forni e dall'alternanza delle fasi di vuoto/plasma. La campagna sperimentale è stata effettuata principalmente in gas idrogeno, gli ultimi due giorni in deuterio. I dati analizzati in presenza di deuterio mostrano che l'erosione di cesio è molto più evidente (si trova il triplo della densità di cesio nella sorgente), mentre la densità rilevata in funzione dell'evaporazione dai forni è invariata rispetto alle operazioni in idrogeno.

Abstract

Nuclear fusion is among the most ambitious energy production research areas of the future with low environmental impact. Currently, the world's largest controlled thermonuclear fusion experiment is under construction in Cadarache, southern France: ITER. In order to achieve the ideal performance for nuclear fusion in ITER, additional heating systems are required. Injection of beams of neutral particles is among the most important methods. At the RFX Consortium in Padua, experiments are underway on SPIDER (Source for Production of Ion of Deuterium Extracted from Rf plasma), the prototype of the negative ion source that will be used in neutral injectors. Negative ions are instrumental in the production of neutral beams, whose current must be maximised in order to bring the central plasma temperature inside ITER to 10 keV–15 keV.

One of the main results to be achieved by SPIDER is a current density of negative ions H^- of $355\,\mathrm{A m^{-2}}$ and ions D^- of $285\,\mathrm{A m^{-2}}$. To achieve these goals, it is essential to evaporate caesium within the source. Caesium lowers the surface work function so as to increase the conversion of ions and atoms into negative ions; it is therefore of paramount importance to monitor caesium density and distribution within SPIDER. The diagnostic system used to monitor the density and uniformity of neutral caesium is Laser Absorption Spectroscopy (LAS). This thesis focuses mainly on this one by improving the density estimates made in the 2021 experimental campaign and deepening the knowledge on the distribution of caesium inside SPIDER under vacuum and plasma conditions.

The results obtained from the analysis show that caesium is mainly distributed in the upper-middle part of the source and its presence is strongly dependent on oven evaporation and vacuum/plasma phases. The experimental campaign was carried out mainly in hydrogen gas, the last two days in deuterium. The data analysed in the presence of deuterium show that the erosion of caesium is much more pronounced (the caesium density in the source triples), while the density measured as a function of evaporation from the ovens is unchanged with respect to operations in hydrogen.

List of Acronyms

AG	Acceleration Grid	5
BP	Bias Plate	6
CATS	CAesium oven Test Stand	12
D-T reaction	Deuterium-Tritium reaction	1
EG	Extraction Grid	5
HNBI	Heating Neutral Beam Injectors	4
LAS	Laser Absorption Spectroscopy	8
LoS	Lines of Sight	8
NBI	Neutral Beam Injectors	1
OES	Optical Emission Spectroscopy	10
PG	Plasma Grid	5
RF	Radio Frequency	1
SPIDER	Source for Production of Ion of Deuterium Extracted from RF plasma	1

Table of contents

1 Introduction

The thesis study carried out at the RFX Consortium is here presented. Section 1.1 briefly introduces the fusion energy production with some insight of its advantages as a new future source of energy. Section 1.2 concisely describes the ITER project, focusing on its heating system. Section 1.3 presents the Source for Production of Ion of Deuterium Extracted from RF plasma (SPIDER) with a short description of Neutral Beam Injectors (NBI) sources. Finally, Section 1.4 focuses on the structure of the Radio Frequency (RF) negative ion source, with specific interest in the caesium ovens and all the grids employed to the negative ions extraction.

1.1 The role of fusion energy in the energy production mix

The world's electricity consumption per capita has continuously grown over the past half a century. Between 1980 and 2018, electricity consumption has grown from 2.1 MW h per capita to 3.3 MW h per capita [1]. Due to various events in the international context, the global electricity demand in 2022 showed a slower growth of 2.4% compared to 2021 and similar growth rates are expected for 2023, showing that the demand has anyway a positive growth of 2% [2]. Furthermore, considering the challenges related to climate change, finding new innovative solutions to produce energy, with low environmental impact, is crucial. ITER will be the first fusion nuclear project built to regularly operate with a relatively high rate of fusion reactions so as to have a net production of fusion energy. The final goal is to generate 500 MW of power associated to fusion reactions from 50 MW of input power. ITER itself will not produce electricity for commercial purpose, but will be fundamental to test key physical and technological aspects of future commercial reactors [3].
Fusion reaction is a physical phenomena where two light nuclei fuse together to form a heavier element. This process leads to an energy release, due to the mass difference between the reactants and the products. One example of fusion reaction is presented in Eq.1:

$$^{2}\mathrm{H} + {}^{3}\mathrm{H} \longrightarrow {}^{4}\mathrm{He}(3.5\,\mathrm{MeV}) + \mathrm{n}(14.1\,\mathrm{MeV}) \tag{1}$$

known as *Deuterium-Tritium reaction (D-T reaction).* When Deuterium (^{2}H) and Tritium (^{3}H), both isotopes of hydrogen, are fused together they form an atom of helium (^{4}He) and a neutron (n); the mass difference Δm is related to an energy release of 17.6 MeV according to Einstein relation $\Delta E = \Delta m\, c^2$. The energy ΔE is the difference between the *binding energy* of the nuclei of reactants and products. Therefore, when an atom (e.g. helium), more bounded than the atoms that are fused together (e.g. deuterium and tritium), is formed, an exoenergetic (on a microscopic scale) and exothermic (on a macroscopic scale) process takes place. As about 80% of this energy goes into the neutron, electricity can be generated through conventional steam turbines using the heat deposited in a neutron absorbing material. From Eq.1 it can be pointed out that the first advantage of fusion lies in its fuel. Deuterium is found mixed up (1 part in 6000) as heavy water (D_2O), while tritium (which is rather rare) can be bred inside the reactor from lithium, as shown in Eq.2:

$$\mathrm{n} + {}^{6}\mathrm{Li} \longrightarrow {}^{4}\mathrm{He}(2.1\,\mathrm{MeV}) + {}^{3}\mathrm{H}(2.7\,\mathrm{MeV}). \tag{2}$$

Thus, the availability of fuel for fusion reaction is expected to last tens of thousands of years [4]. The formula shown in Eq.1 is the most convenient fusion reaction amongst the many different possibilities. In fact D-T reaction has the largest cross section per incident particle energy, compared to the others illustrated in Fig.1. In this way less energy is required (i.e. the heat required to start fusion) for this mixture to have the highest probability for fusion to happen. Fig.1 shows that D-T reaction (in red) has the maximum peak at the lowest incident particle kinetic energy, around 100 keV. This entails two main advantages; the first implies that ITER will be fuelled with a D-T mixture, as it requires lower plasma temperature compared to the other reactants, as shown in Fig.1. The second advantage is that radioactive waste in fusion power plants mostly comprises Low-Level Waste (LLW) and Intermediate Level Waste (ILW) [5], which have limited environmental impact. As a matter of fact, the only radioactive element in Eq.1 is tritium (^{3}H) -a weak beta emitter (18.6 keV maximum energy)- whose radiation can be absorbed by a thin sheet of paper [6]. The main criticality is represented by neutron activated reactor components, that will be the only radioactive waste. Fusion reactors are designed carefully with low activity materials so as to require containment of less than one hundred years after decommissioning. Lastly, the amount of CO_2 emissions from the life cycle of fusion power plant is one of the lowest when compared to various fuel resources, as shown in Fig.2. Therefore, fusion power is expected to play an essential role to reduce green-house gas emissions from energy production in the future.

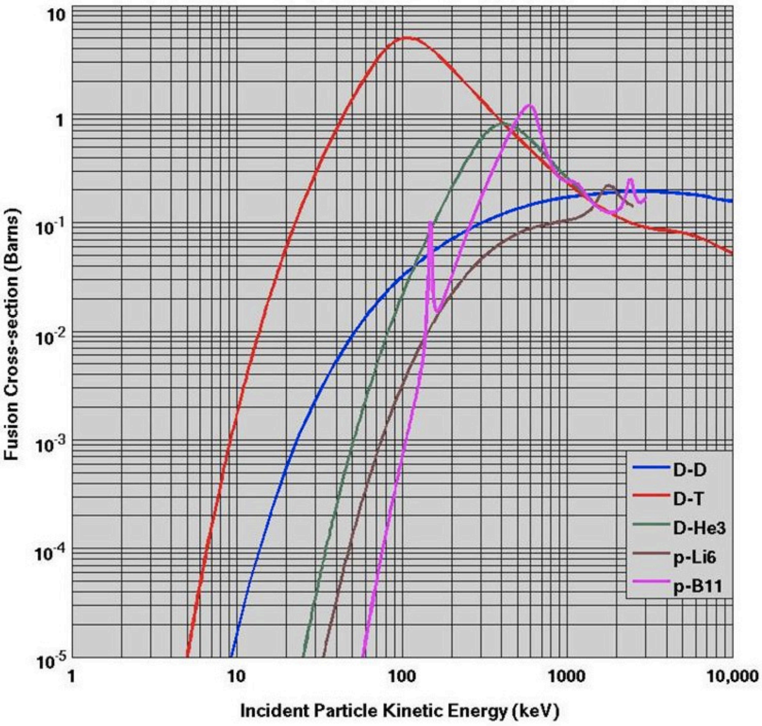

Figure 1: Cross-sections of different fusion reactions of kinetic energy of an incident deuterium or proton on a stationary target.

1.2 ITER

In order for fusion to occur, protons (or heavier nuclei) have to be brought close enough to overcome the electrostatic repulsion between them and let the nuclear strong force take over so as to fuse them together. In nature examples of fusion reactions can be found in the sun, where gravity alone is so strong that it is able to trigger the nuclear fusion of its constituents, i.e. hydrogen and helium. While this normally occurs in the stars, there is a “human size” option to recreate nuclear fusion condition: heating the nuclei to very high temperatures ($\approx 10^8$K) so that the kinetic energy is sufficient to overcome the electrostatic repulsion and make them close enough to fuse. The state of matter of the fusion reactants, in the form of highly ionised gas at such temperature, is known as *plasma*. The plasma in ITER needs to be confined for a sufficient period of time away from any surrounding walls so as to keep its integrity. In the first place the vessel is many orders of magnitude cooler than the plasma, consequently any contact between them would cool down the plasma. Furthermore, the surrounding wall particles, after

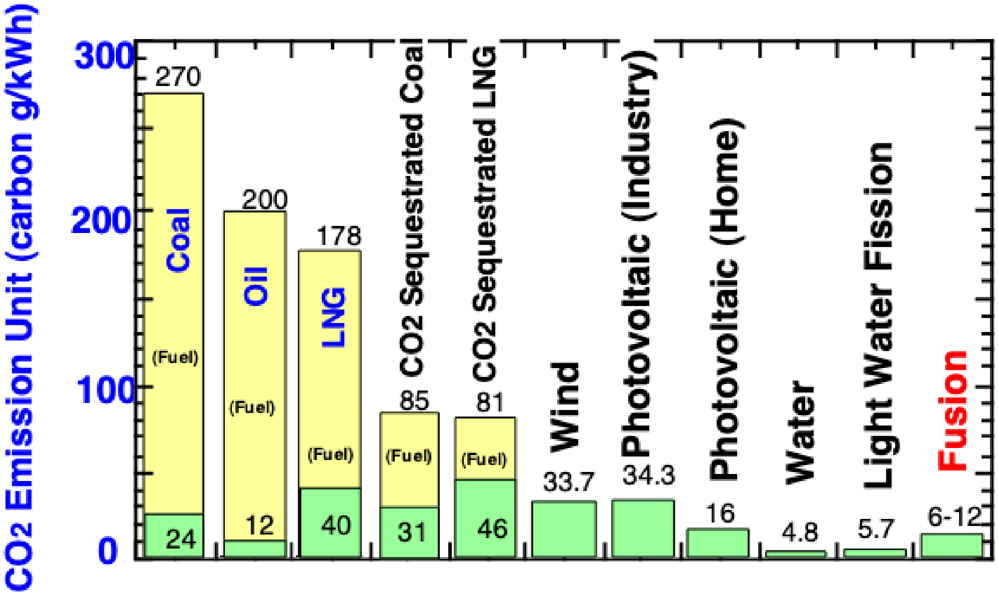

Figure 2: CO_2 emission units for coal, oil, Liquefied Natural Gas (LNG) fired powers, CO_2 sequestrated coal, CO_2 sequestrated LNG fired powers, wind power, photovoltaic power, water power, fission power and fusion power generation [6].

being eroded, would dilute the plasma, resulting in cooling it down. These are the main reasons why plasma may not reach the fusion condition. Moreover, there is no material or technology available that could tolerate the consequent heat flux. One way to confine the plasma is through *magnetic confinement*, which takes advantage of the electromagnetic properties of plasma; this is the approach that will be used in ITER.

ITER, currently under construction in southern France, will be the largest fusion reactor ever built. It will feature a *tokamak* magnetic confinement configuration. The geometry configuration of a tokamak is described by a *torus*: a surface generated by revolving a circle in three-dimensional space about an axis located outside the circle. The tokamak magnetic configuration is formed by two magnetic fields: the *toroidal* linked with the *poloidal* one. The first is induced by a set of ring-like coils placed in a torus shape and the latter is formed by the toroidal current flowing within the plasma itself, as shown in Fig.3.

In the torus, there are two pressure forces balancing each other: the magnetic one opposed to the plasma pressure. With the current level of technology available, cryo cooled superconducting coils can reach a maximum magnetic field of 11.8 T within the torus [3]. Usually the ratio between plasma pressure (also known as *kinetic pressure*) and magnetic pressure is referred to the *Beta parameter*:

$$\beta = \frac{p_{\mathrm{kin}}}{p_{\mathrm{mag}}} = \frac{nk_BT}{B^2/(2\mu_0)}.$$

where n is the number density, k_B is the Boltzmann constant, T is the temperature, B is the strength of the magnetic field and μ_0 is the vacuum permeability. The plasma β gives an idea of the efficiency of magnetic plasma confinement and for fusion plasma is in the order of 1%, meaning that the magnetic pressure is much greater than kinetic pressure.

The plasma in ITER will be heated in different ways, all combined together. The first one is **Ohmic heating**, generated within the tokamak itself. The central solenoid of ITER induces an electrical current in the torus. The result of this flow of current is heat because the plasma has a finite resistivity. The latter depends on the temperature T, more precisely as a function of $T^{-3/2}$, consequently the efficiency of ohmic heating is not enough at reactor-relevant temperatures (10 keV–20 keV), so other forms of external heating are necessary:

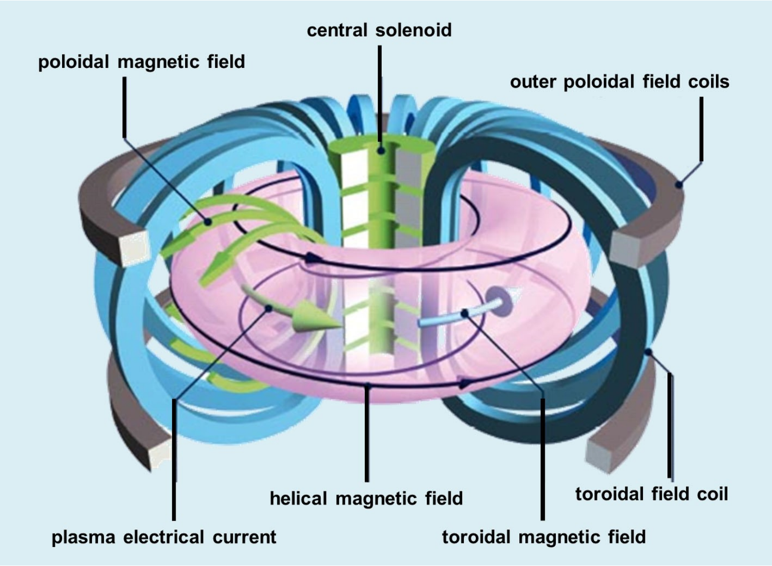

Figure 3: Inside view of ITER tokamak, the blue and grey components represent the superconducting magnets. The plasma chamber has a external radius of 6.2 m and internal radius of 2 m for a total plasma volume of 840 m^3.

- **Power radiofrequency sources**: radiowaves are injected in order to excite specific resonances (e.g. cyclotron resonances) of electrons, ions or of the whole plasma.
- **NBI**: one of the most convenient solutions to heat a dense plasma is by injecting beams of high energetic neutral particles, with a beam energy much above the average kinetic energy of the plasma electrons or ions (ca. 0.04 MeV–1 MeV).

Due to the presence of strong magnetic fields, injecting charged particles would be problematic. Neutral particles are not affected by magnetic fields, hence they can penetrate, at the right depth, the plasma and transfer energy to it. The structure of NBI will be better described in the following section. ITER will initially be equipped with two Heating Neutral Beam Injectors (HNBI) that are designed to deliver 33.3 MW to the plasma for up to 3600 s; a third one may be installed later [7]. Therefore, NBI sources play a crucial role to make fusion reaction possible.

1.3 SPIDER

The full-scale NBI source prototype SPIDER for ITER is operating at the Neutral Beam Test Facility, located at the RFX Consortium in Padua (Italy). To satisfy the requirements for ITER mentioned in Section 1.2, SPIDER will have to succeed at many demanding tasks. No other NBI has achieved all these requirements simultaneously before. Some of the most important ones are listed in Table 1.

The reason for using ion sources in order to produce neutral beams is essentially the fact that neutral particles cannot be accelerated. Therefore, the principle of NBI is producing negatively or positively charged ions that are accelerated (up to 100 keV), neutralised and finally injected into the tokamak to heat the plasma. These ions are created in a plasma source, then they are accelerated to the desired energy. After acceleration, the ions go through a neutraliser cell where a fraction of them is converted into neutral particles by *charge exchange processes* with the neutral background gas (H_2 or D_2). As not all of the ions are neutralised in this process, a potential of -20 keV is applied after the neutralisation cell so that the ions entering the channels are deflected left or right, depending on their charge [7]. Fig.4 shows a scheme of a NBI. This short description applies both to negative and positive ions. In the 1970s

Table 1: Performances required for SPIDER [8, 9].

Source H_2/D_2 pressure	$< 0.3\,\mathrm{Pa}$
Energy of the ions	$100\,\mathrm{keV}$
Pulse duration	$3600\,\mathrm{s}$ (D) $1000\,\mathrm{s}$ (H)
Beam homogeneity	$> 90\%$
Extracted current density	$285\,\mathrm{Am^{-2}}$ (D) $350\,\mathrm{Am^{-2}}$ (H)
Current density ratio of electrons to ions accelerated	$j_e/j_{D^-} < 1$ $j_e/j_{H^-} < 0.5$

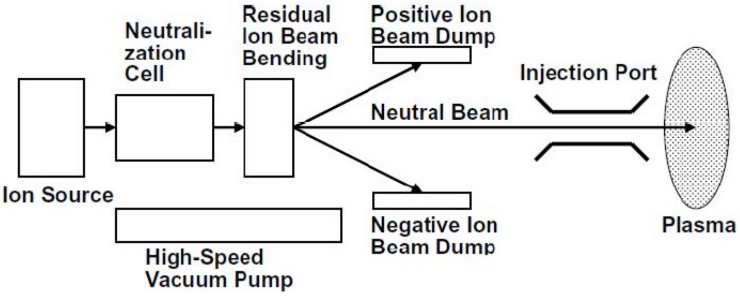

Figure 4: Schematic of a Neutral Beam Injector (NBI) [4].

and 1980s large positive ion sources were developed in large fusion reactors such as JET[1] and TFTR[2]. However, it was discovered that the neutralisation efficiency for negative H^-/D^- ions, at energy higher than 150 keV per nucleon, remains 60%. Whereas for positive ions it drops to few percent, hence the propensity for negative ion sources to be used in ITER NBIs [4].

1.4 Ion Source

SPIDER hosts a negative ion RF source whose principal components are illustrated in Fig.5. The RF ion source is located in the rear part of SPIDER and it is the component where the negative ions are generated. Inside the RF ion source there are eight small alumina cylindrical plasma sources, called *drivers*. A driver is an Inductive Coupled Plasma (ICP) source which creates a partially ionised plasma receiving energy from a coil surrounding the cylinder; the adopted radiofrequency is about 1 MHz. The generated plasma then diffuses in an expansion region. Around the plasma chamber a system of permanent magnets creates a multicusp magnetic field that reduces plasma losses. The ions are formed in the plasma chamber by dissociative attachment of the vibrationally excited hydrogen molecules, produced during the collisions between low energy electrons ($\approx 4\,\mathrm{eV}$), as described in Eq.3:

$$H_2 + e_{\mathrm{fast}}(> 10\,\mathrm{eV}) \longrightarrow H_2(\nu) + e \longrightarrow H_2(\nu) + e_{\mathrm{slow}}(< 4\,\mathrm{eV}) \longrightarrow H^- + H \tag{3}$$

where $H_2(\nu)$ represents the vibrationally excited hydrogen molecule. The chain reaction presented in Eq.3 is known as *volume production*, because the negative ions are produced inside the plasma volume. Facing the expansion region there are three grids, in order: Plasma Grid (PG), Extraction Grid (EG) and Acceleration Grid (AG), through which the negative ion beamlets are extracted from the ion source and accelerated up to 100 keV. Each grid features 1280 apertures.

---

[1] *Joint European Torus* in Culham, Oxfordshire (UK).

[2] *Tokamak Fusion Test Reactor* in Princeton, New Jersey (US).

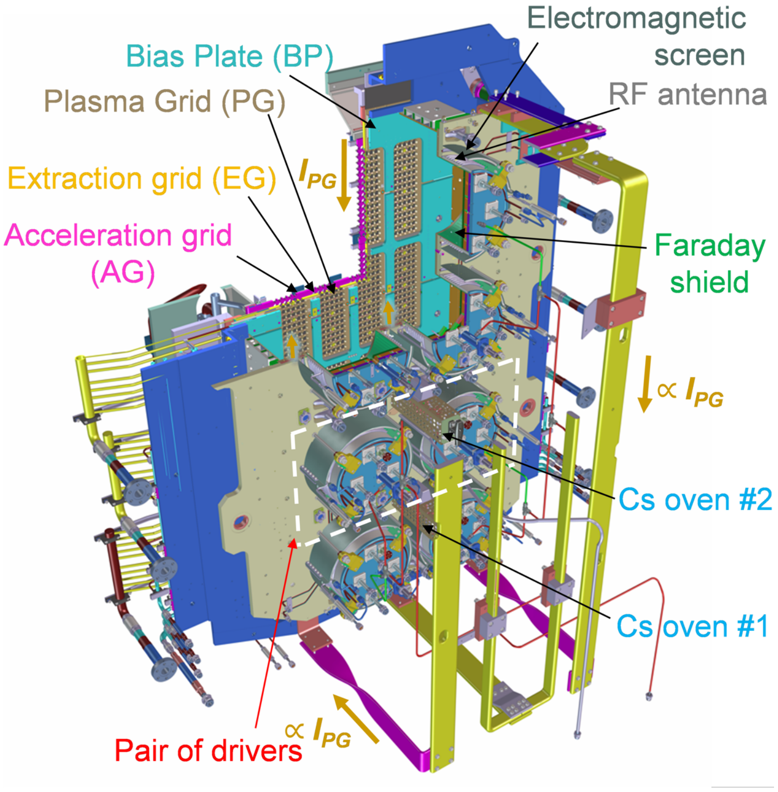

Figure 5: Overall section view of the SPIDER ion source [10].

Alone, the reactions described in Eq.3 are not sufficient to satisfy the H^-/D^- demand, so a *surface production* is added in order to significantly increase the negative ion production yield by about one order of magnitude. This method consists in covering the PG, whose surface is made of molybdenum coated copper, with a monolayer of caesium. In this way, the work function of the cesiated PG surface reaches a minimum around 1.4 eV–1.8 eV at 0.5–0.8 monolayer depending on the substrate material and on the crystallographic orientation [11]. The work function then increases again, until the bulk Cs work function of 2.1 eV is obtained and maintained for coverages above few monolayers [12]. As a matter of fact, the atoms in the plasma (e.g. H and H^+) impact on the PG, layered with caesium, and pick up the extra electron turning into H^-. Afterwards, these negative ions are backscattared from the PG surface into the plasma, pushed back towards the PG again by Coulomb collisions with the plasma ions and accelerated passing through the apertures in the PG.

To avoid losses of H^- or D^-, a magnetic filter field (10^{-2}T) is added nearby the PG. Its function is mainly twofold: to lower the electron density n_e ($\approx 10^{17}\text{m}^{-3}$) and particularly the electron temperature T_e near the PG (below 2 eV) in order to counteract the electron detachment processes, which could significantly reduce the amount of negative ions available for extraction. Furthermore, some of these electrons, present in the plasma volume, are co-extracted and are accelerated together with the negative ions. These coextracted electrons represent a serious problem both for negative ions and for the components of SPIDER. A too high amount of them would cause a thermal load on the latter, resulting in serious damages. Indeed, a crucial target in the operation of a negative ion source is keeping the ratio of extracted electrons and ions as low as possible, as indicated in Table 1.

The above mentioned magnetic filter field is generated in SPIDER by a current flowing vertically in the plasma grid I_{PG}. The latter generally flows downwards (though occasionally the direction has been reversed) and it is between 1 kA and 5 kA giving values of magnetic field, going transversely to the expansion region, respectively of 1.6 mT up to 8 mT close to the PG. Facing the PG, there is the Bias Plate (BP); it is disposed in such a way as to cover the border

of the PG surface exposed to the expansion region. The aim of the BP is additional to the magnetic filter field. The BP indeed is positively biased, as well as the PG, against the body source in order to reduce the rate of coextracted electrons. This bias generates an electric field diminishing the amount of electrons that could get sufficiently closer to the PG apertures and be co-extracted together with the negative ions. The biasing of PG and BP against the source body potential is performed respectively by the Ion Source BIas (ISBI) and the Ion Source Bias Plate (ISBP) power supplies, which are normally current-regulated to control the net flux of removed electric charges [13]. In front of the PG is located the EG, which is the first responsible of the acceleration stage. In the first place, ions and the residual electrons are extracted by applying an extraction voltage up to 12 kV between the plasma and the EG. Permanent magnets are embedded in the EG to deflect the residual electrons out of the beam, onto the EG surface. Negative ions are barely affected by the resulting magnetic field, due to their mass which is way higher than the electron one, and can thus pass through the extraction grid almost unaltered.
Lastly, there is the AG kept at ground potential which terminates the negative ion acceleration stage. Fig.6a illustrates all the grids, recently described, that the ions encounter in their path, from their creation to acceleration and extraction of the H^- alone.

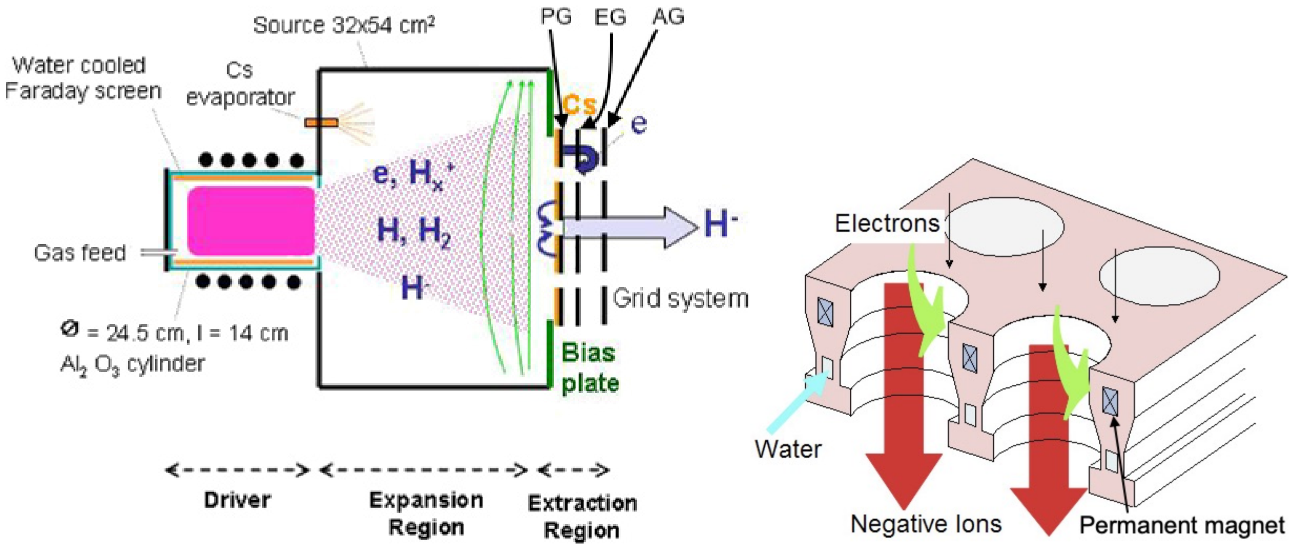

(a)

(b)

Figure 6: Fig.6a shows the schematic concept of a RF negative ion source; Fig.6b illustrates a schematic view of an Extraction Grid [14, 15].

As mentioned before, the PG is layered with caesium to enable surface production. Fig.7 shows, for the case of an arc discharge current ion source, that evaporating caesium (Cs) increases negative ion production yield significantly; moreover its presence along the PG is also essential to guarantee the uniformity of the beam current [16].
Cs is evaporated inside the plasma chamber by means of three ovens installed in the rear side of the negative ion source. Each one contains 10 g of Cs. Fig.8 illustrates an inside view of the ovens; the nozzle is the only part that goes inside the chamber. The reservoir contains the caesium, which is heated by multiple heaters placed in it and all along the duct. This duct is heated in such a way as to have a growing temperature gradient from the oven to the injection tube. All this is necessary to minimise the build-up of any cold spots that might be inside the oven. In order to maintain the rate of production of negative ions, fresh caesium has to be deposited almost continuously inside the chamber. In addition, as the seeding of Cs on the PG surface has to be uniform, these devices are placed at different heights on the ion source to allow

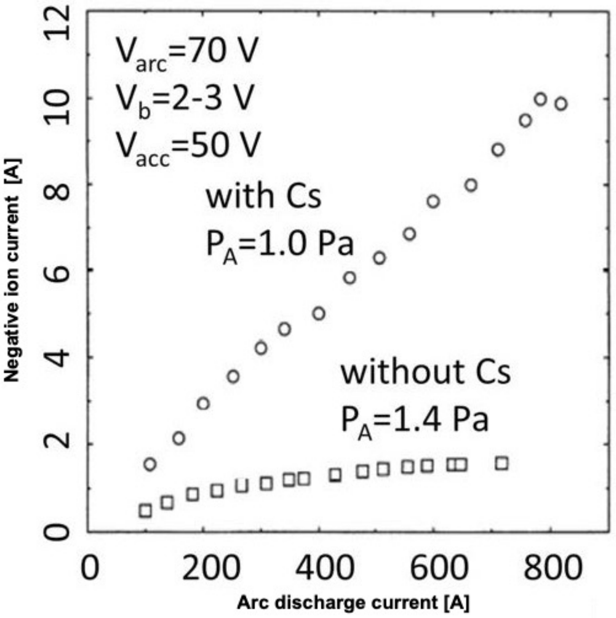

Figure 7: Effect of caesium seeding in the JAERI 10 A negative ion source at different working gas pressure P_A. Negative ion current I_{H^-} on the ordinates grows considerably in presence of Cs [17].

control of the caesium distribution [18]. For this purpose a Surface Ionisation Detector (SID) is embedded in the nozzle of the ovens, which can give an estimate of the caesium evaporation rate of the ovens [19].
Caesium is an alkali metal, so it is extremely reactive with any impurities that might be in the chamber (like oxygen and nitrogen); as such it must be kept isolated from the atmosphere and from poor vacuum conditions. Considering that Cs liquefies at about 28°C, a temperature control of the plasma chamber and of the PG is required to avoid uncontrolled depositions of caesium. Experiments in other negative ion sources showed that the optimal caesium deposition is reached by keeping the body of the chamber at 40°C and the PG[3] between 120 °C–150 °C [20]. Lastly, parallel to the PG surface the Lines of Sight (LoS) of the Laser Absorption Spectroscopy (LAS) diagnostic have their origin, in order to actively monitor the caesium density. The purpose and the diagnostic of the LAS will be more suitably examined in the next section as it represents the main core of the thesis work.

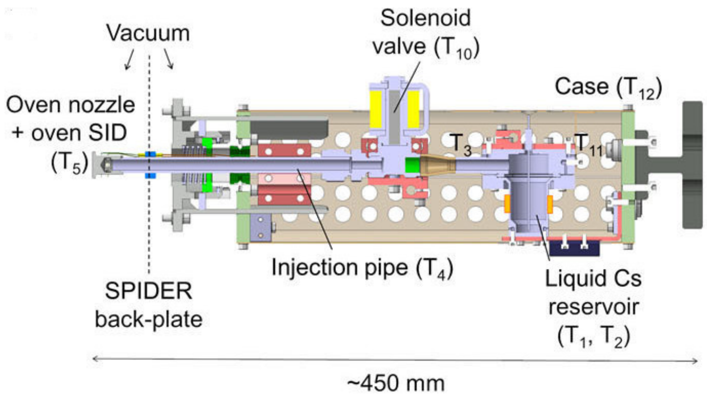

Figure 8: 3D model of the caesium oven main components and thermocouple positions [21].

From what has been said so far, it follows that it is extremely important to study the presence of caesium to enhance the knowledge of its effect in the presence of plasma and how to optimize

---

[3] By design the PG in SPIDER can not exceed 125°C of temperature.

its deposition on the PG. As such, this thesis will concentrate particularly on these topic: 1) by improving the analysis of the data collected during the LAS 2021 campaign, 2) by studying and monitoring caesium density and spatial uniformity and 3) by evaluating caesium relation to the fundamental parameters of SPIDER.

2 Laser Absorption Spectroscopy

This section introduces the principal experimental setup and diagnostic used during the data acquisition. Section 2.1 presents the main features of LAS diagnostic setup, whereas Section 2.2 provides a summary of the physical concept behind laser absorption spectroscopy.

2.1 Experimental and diagnostic setup

Cs plays a fundamental role in enhancing negative ion yield production. The two diagnostics built to actively monitor the presence of caesium inside the ion source are: Optical Emission Spectroscopy (OES) and LAS. The first one detects the amount of Cs in different areas of the source by looking at the emission spectrum of several caesium lines. However, quantifying Cs from emission lines requires the knowledge of different plasma parameters (such as electron temperature T_e and density n_e) and the availability of a collisional-radiative model, which is subject to the uncertainties on the cross sections of all the involved reactions. Furthermore, during plasma phase small amount of caesium is sputtered away from the PG and some other is partly ionised in the chamber; this influences the intensity of the Cs emission spectrum lines. The second diagnostic, LAS, can give a direct access to the ground state density n_k of caesium both in vacuum and plasma phase without interference in the measurements. Fig.9 shows an outline of LAS.

LAS diagnostic consists of a finely tunable laser, which is shot into a cable fibre and crosses the ion source parallel to the PG. The laser beam diameter in the cable fibre is approximately 3.6 mm. A single mode Distributed FeedBack (DFB) diode, with a total tunable range 851 nm-853 nm, a spectral line width of 0.01 pm and a maximum output power of 60 mW, produces the laser light. After being emitted by the laser system, the light goes to the attenuator, which can vary the available laser power, and then is guided to a 7 m long single mode fiber. Before entering through SPIDER, the optical fibre is splitted in four, making up four laser beams and consequently the same amount of LoS, which are horizontally oriented at different heights to provide the spatial distribution of Cs along the PG. The distance of each laser beam from the PG can be modified from 5 mm to 65 mm [22]. Indeed there are several possible lines of sight, defined by the holes placed on the sides of the source, where the light of the laser can pass through at 5 mm and 25 mm distance from the upstream faces of BP and PG.

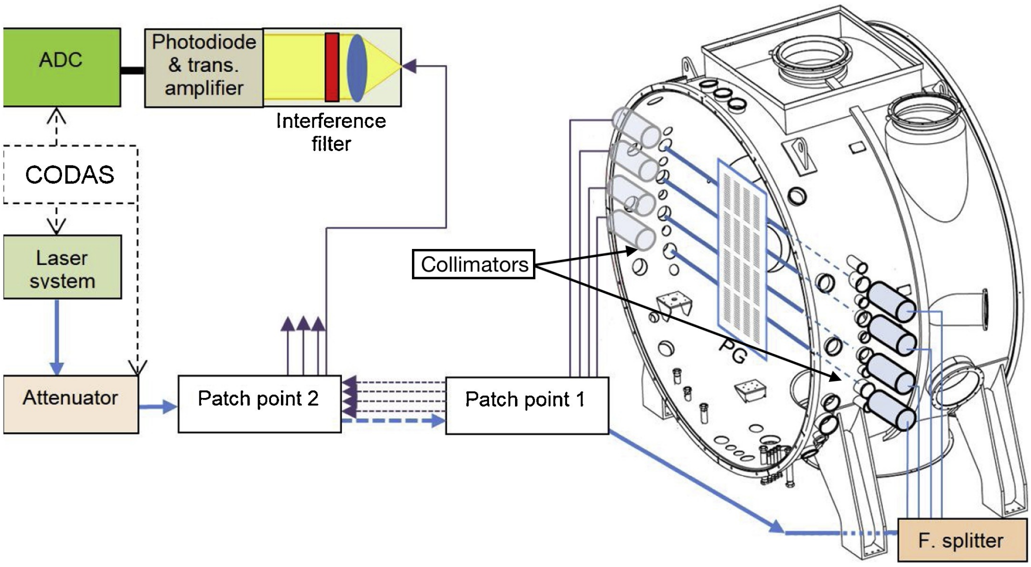

Figure 9: LAS diagnostic inside SPIDER [22].

Fig.10 shows the disposition of the four LoS in relation to the source. On the left the vertical section of both the source and of the acceleration system of SPIDER are shown, together with the electrical scheme of the main power supplies described in Section 1.4. On the right, instead, the position of the LoS is schematically shown with respect to the BP (light blue) and of the PG, as seen from the back of the source. The diode (DFB) and the attenuator are managed by a dedicated controller connected to the SPIDER COntrol Data Acquisition System (CODAS). The light of the four lasers is then collected by the same numbers of collimators, which guide the light through four fibre cables into the two patch points and to the diagnostic control room. In the control room the intensity of the laser light is measured by a 16 mm^2 active area of the `OSI OSI020-UV` amplified photodiode, which converts the power of the laser in a voltage signal. An interference filter, placed before the photodiode, stops spurious light that might come from the plasma, i.e. blocks all the light except in a range of very few nm around 852 nm. This output voltage signal is eventually amplified with a gain 1/10/100/1000 and digitised by the same CODAS system previously mentioned.

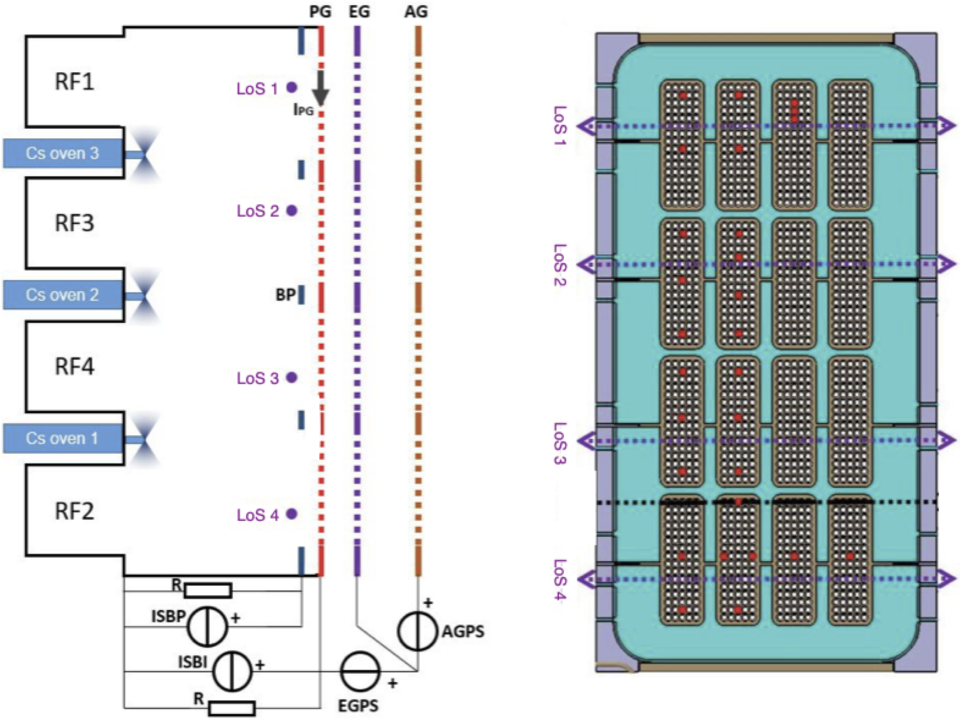

Figure 10: Disposition of the four LoS, as seen from the side of the source (on the left) and from the back (on the right) [13].

2.2 LAS absorption physics theory

As mentioned in Section 2.1, the laser has a tunable range between 851 nm-853 nm. The reason for having exactly this range can be found in the atomic proprieties of Cs. Caesium has a $5p^6 6s$ ground state electronic configuration, resulting in a $6\,^2\mathrm{S}_{1/2}$ state in Russell-Saunders notation[4]. The first excited configuration instead is $5p^6 6p$. This new configuration leads to two fine structures, $6\,^2\mathrm{P}_{1/2}$ and $6\,^2\mathrm{P}_{3/2}$. The transitions from $6\,^2\mathrm{P}_{1/2}$ and $6\,^2\mathrm{P}_{3/2}$ to the ground state correspond to the D_1 line at 895.3 nm and the D_2 line at 852.1 nm, respectively [23]. Due to the lower wavelength of the D_2 line, which implies a better availability of light sources and sensitivity of detectors, this transition has been chosen for absorption spectroscopy.

The intensity $I(\lambda, L)$ of the light coming out of an absorbing medium, which in this case is

---

[4] In RS notation coupling atomic states are described like $^{2\mathrm{S}+1}\mathrm{L}_\mathrm{J}$, where S, L, J are the total spin, orbital and angular momentum quantum number, respectively.

Cs, with length L is correlated to the intensity of the light beam $I(\lambda, 0)$ and the absorption coefficient $c(\lambda)$ according to the differential equation presented in Eq.4:

$$\frac{dI(\lambda, x)}{dx} = -c(\lambda)\, I(\lambda, x) \quad \overset{(a)}{\Rightarrow} \quad I(\lambda, L) = I(\lambda, 0)\, e^{-c(\lambda)L} \tag{4}$$

where in (a) it has been integrated over a path of generic length L, with $L = 0.87\,\mathrm{m}$ being the length of the laser beam path inside the cesiated source in SPIDER. The wavelength integrated absorption coefficient $c_{ki}(\lambda)$ for transition $k \to i$, where k indicates the lower state and i an upper state, follows the relation presented in Eq.5 [24]:

$$\int_{\text{line}} c_{ki}(\lambda) d\lambda = \int_{\text{line}} n_k \frac{g_i}{g_k} \frac{\lambda_0^4}{c} \frac{A_{ik}}{8\pi} L_p(\lambda) d\lambda = n_k \frac{g_i}{g_k} \frac{\lambda_0^4}{c} \frac{A_{ik}}{8\pi}. \tag{5}$$

where n_k, the desired parameter, represents the population density of the ground state, g_i and g_k the statistical weights of upper and lower level, c is the speed of light, $\lambda_0 = 852.1\,\mathrm{nm}$ is the aforementioned D_2 line wavelength and A_{ik} the Einstein transition probability for spontaneous emission. $L_p(\lambda)$ describes the normalised profile line ($\int_{\text{line}} L_p(\lambda) d\lambda = 1$).
Deriving the absorption coefficient $c(\lambda)$ in relation to the intensities $I(\lambda, L)$ and $I(\lambda, 0)$ from Eq.4 and substituting it in Eq.5, the ground state density for resonances lines is obtained according to the relation presented in Eq.6:

$$n_k = \frac{8\pi c}{\lambda_0^4} \frac{g_k}{g_i} \frac{1}{A_{ik} L} \int_{\text{line}} \ln \left[\frac{I(\lambda, 0)}{I(\lambda, L)} \right] d\lambda. \tag{6}$$

With a view to validate the accuracy of n_k, before the SPIDER caesium campaign in 2021 LAS diagnostic was installed in the CAesium oven Test Stand (CATS) ovens, to carry out tests and preliminary experimentation on the caesium ovens, mentioned in Section 1.4. The experimental setup parameters of CATS are very similar to the one installed in SPIDER so these preliminary results were able to give useful outcomes to be used in the SPIDER data analysis. The target of CATS experiment was monitoring the Cs evaporation from the oven while simultaneously testing LAS diagnostic components [22]. Fig.11 shows the photodiode signal as ideally expected, illustrating the ramp of the signal interrupted by two peaks composing the D_2 line. As shown in the figure, the D_2 transition splits in two distinct peaks; this is a consequence of the *hyperfine structure*. Fundamentally, due to the presence of nuclear spin and according to the selection rules for optical transitions, the D_2 emission line consists of 6 hyperfine lines. Specifically, the ground state $6\,^2\mathrm{S}_{1/2}$ splits up into two hyperfine levels ($F = 3, 4$ being F the total angular momentum quantum number of the atom) and the chosen excited state $6\,^2\mathrm{P}_{3/2}$ into four hyperfine levels ($F = 2, 3, 4, 5$). According to the optical selection rules, i.e. $\Delta F = 0, \pm 1$, the 6 hyperfine lines permitted are the pairs of F numbers shown in Fig.12. Doppler broadening of these individual lines cause an overlap of these 6 lines resulting in two peaks, with a Gaussian like profile separated from each other by $\Delta\lambda = 21.4\,\mathrm{pm}$ as seen in Fig.12.
The CATS experiment has revealed that the Cs density lies in a range between $10^{13}\mathrm{m}^{-3}$ and $10^{16}\mathrm{m}^{-3}$, depending on the line saturation condition. This result can give a lower and upper estimate of the Cs density for the SPIDER experimental campaign. The measurement uncertainties are 2 %–5 %, but can reach 5 %–10 % in the case of line saturation. The results were taken from [22] and [25].

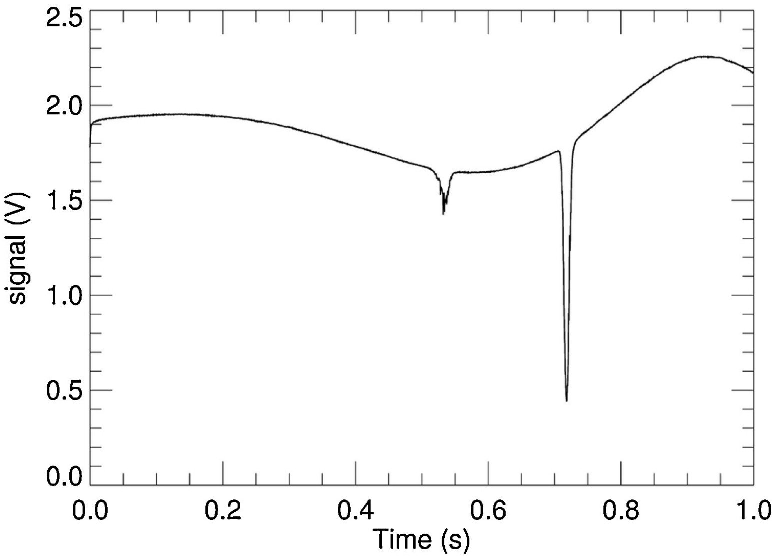

Figure 11: Typical signal of an absorption spectrum of the Cs D_2 line, as acquired by the LAS diagnostic in CATS [22].

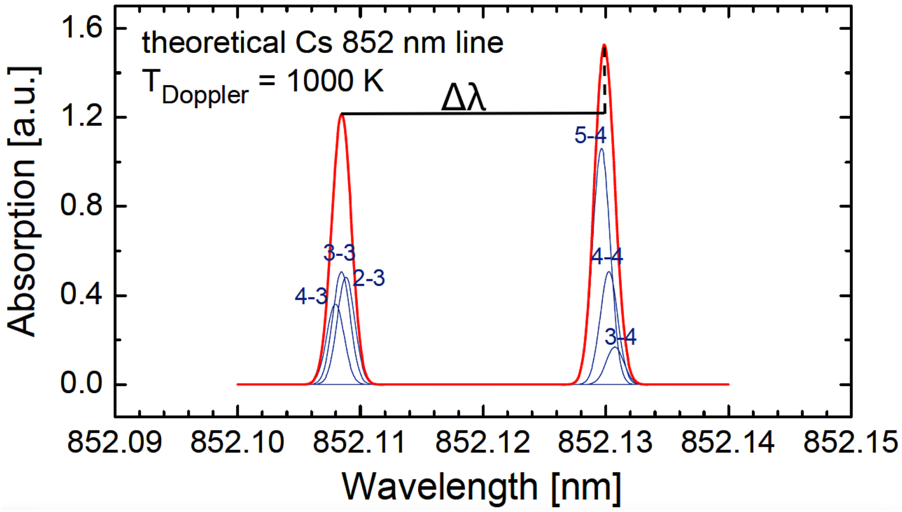

Figure 12: Doppler broadening of the D_2 line at 1000 K. The pairs of numbers (e.g. 4-3, 3-3, ...) represent the hyperfine lines structure of caesium [24].

3 Results

In this section the results of the work carried out during the internship at the RFX Consortium are presented. Section 3.1 briefly describes the numerical methods used to improve the data analysis of the 2021 SPIDER Cs experimental campaign, conducted between May and July 2021, and further analyses. Section 3.2 presents the outcomes of the data analysis about the characterisation of caesium inside the SPIDER in relation with the flux coming out from the ovens, the Cs spatial distribution and vacuum-plasma phase.

3.1 Numerical method

In order to estimate the density of Cs from the LAS data, an algorithm in `IDL` language was already available, however it was improved for accuracy and further analysis. As illustrated in Fig.13, the signals of each LoS is segmented in different ramps, which represent the scanning over time and wavelength of the laser. The voltage output (V) from each amplified photodiode is shown as a function of relative time (t). The LAS diagnostic comprises four LoS: LoS1 is the one placed at the top and LoS4 at the bottom of the RF ion source, as shown in Fig.10.

In the first place, the algorithm downloads the data by means of the `MDSplus` platform; thanks to the laser modulation signal, the photodiode signal is divided into portions, each one corresponding to a time scan of the laser wavelength. Each of these absorption spectra stand for $I(\lambda, L)$ in Eq.6, therefore the only available data correspond to the measurements of the light which has already passed through the caesium.

The signal upstream the vacuum volume, $I(\lambda, 0)$, is not measured but can be estimated from the $I(\lambda, L)$. As such, a 6^{th} degree polynomial fit is applied to each single wavelength; from its residuals the two absorption peaks are identified, the signal around each peak is removed and the fit is repeated. Depending on the experimental conditions and on the laser modulation settings, the extent of signal removed around each peak is set between ±4% and ±8% for the duration of a single laser scan. The obtained polynomial curve is assumed as approximation of $I(\lambda, 0)$, which is used to calculate the logarithm of $I(\lambda, 0)/I(\lambda, L)$. In this way the Cs density n_k from Eq.6 is estimated. In addition to this, a Gaussian fit is applied to the same peaks (this time including the signal intervals previously excluded around the absorption peaks).

The conversion from units of time to wavelength is calculated knowing the $\Delta\lambda = 21.4\,\text{pm}$, i.e. wavelength difference of the two peaks discussed in Section 2.2. This provides two ways of analysing the same spectra and thus have two estimates of n_k. Fig.14 shows how the algorithm estimates the logarithm of the ratio between $I(\lambda, 0)$ and $I(\lambda, L)$. This particular case does not refer to the SPIDER experiments but illustrates a saturated absorption peak, caused by a broad spectral intrinsic baseline of the laser emission. Executing a Gaussian fit also helps to overcome this issue, at the expense of having a lower confidence level because it estimates a curve from a lower number of data.

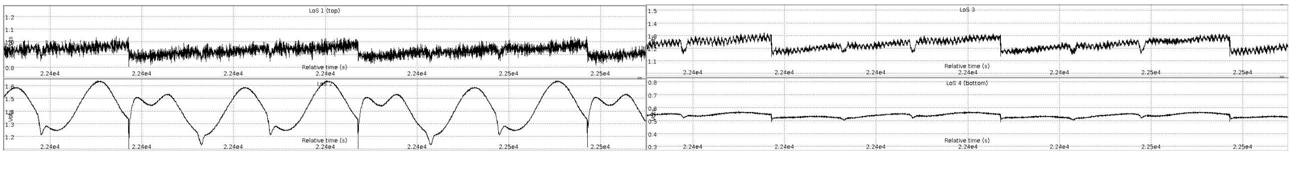

Figure 13: Raw data of the four LoS acquired by LAS in SPIDER, starting from LoS1 in the top left corner to LoS4 in the bottom right. The voltage output V (V) from each amplified photodiode is shown as a function of relative time t (s).

In the beginning the raw data, shown as an example in Fig.13, were inspected through all days of the experimental campaign. Fig.13 also shows that the peaks of Cs detected in SPIDER have a pattern similar to the one shown in Fig.11, indeed the two peaks of the line emission are clearly visible in Fig.13 (except for LoS1). Furthermore, it is evident from Fig.13 that the signal of the first LoS is much more disturbed than the others. This noise is due to mechanical vibration, as the collimators (see Section 2.1) are about four meters apart. As the signals coming from LoS2 are the cleanest one, it was chosen as benchmark to set analysis parameters for all the other LoS. In addition, the peaks are measured all at the same time through the different LoS, i.e. there is no time shift amongst the different LoS.

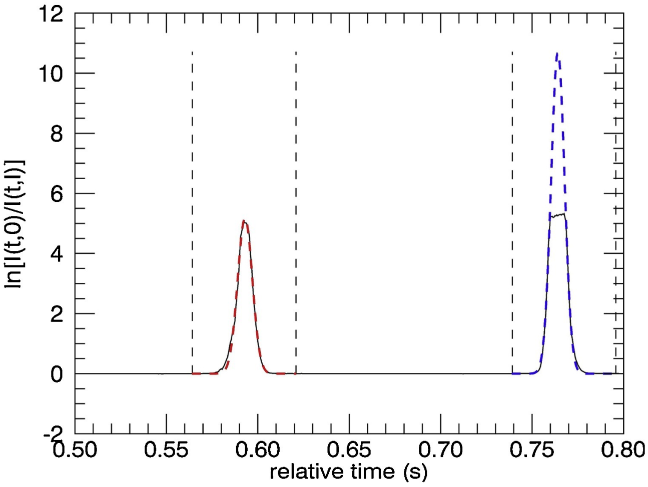

Figure 14: Example of the logarithm of the ratio between $I(\lambda, 0)$ and $I(\lambda, L)$, in a case in which one absorption peak is saturated. The red and blue dashed lines indicate the Gaussian fits on the absorption peaks. Data from the CATS test stand [22].

The main step forward to be done, with respect to the analysis made before this thesis, was to identify the peaks of caesium over the several days of the experimental campaign and improve the analysis of Cs density by fixing specific parameters in the code. Some of these specific parameters included time fixing, i.e. checking if the $\Delta t = t - t_0$ (difference between the time of one peak t and the beginning of the ramp t_0) of the two peaks (within the same LoS) changed, and smoothing the noisy photodiode signals with a moving average filter. The ovens did not evaporate Cs in the source continuously, nevertheless the LAS data acquisition system was left operating and so the peaks of caesium were not always present in the scanning. This is because the density of caesium, after a short period of time (in the order of 5 minutes), becomes too low to be detected by the LAS. These periods of no evaporating caesium correspond to no visible peaks, so these raw data were identified and discarded. When the Cs evaporation persisted long enough (ca. more of one hour), a time shift of the peaks was observed, therefore the Δt aforementioned could increase or decrease during the scanning. This is due to a wavelength drift of the laser which causes a time expansion of the ramps previously shown. In this case, a linear interpolation of the peak times were done and the angular coefficient was used to fix the time shifting. Careful attention was given when there were plasma pulses inside the source. In fact, as mentioned in Section 2.1, during plasma phase small amount of caesium is sputtered away from the PG resulting in absorption peak characteristics, that usually require different analysis settings. In this way the analysis, made in this thesis, is specific for each LoS, distinguishing vacuum phase from the plasma peaks, and takes care of particular cases (like no evaporating caesium and time shifting). The analysis made before, when the campaign was still underway, had the goal to extract approximate values of density to be used as first results of the experiment, and consequently had not the expectation to be as precise as possible (in the short term).

In Fig.15 the spikes, that can be seen, highlight the plasma pulses inside the source. Moreover, the two ways of estimating the Cs density n_k are represented by the red and black line, standing for the Gaussian fit and bare integration respectively.

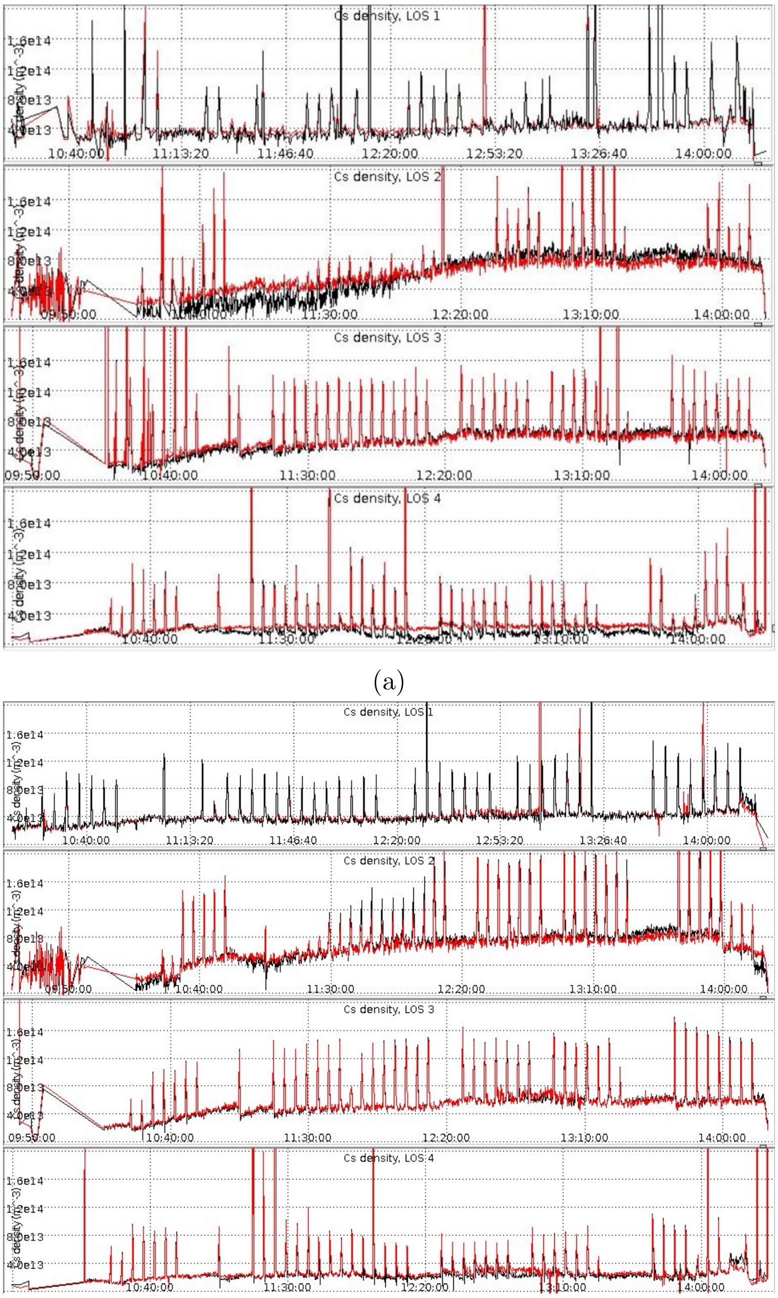

(a)

(b)

Figure 15: Charts of the Cs density n_k (m^{-3}) estimate of one experimental day as seen from the four LoS as a function of absolute time t (h:min:s). Fig.15a corresponds to the analysis made during the experimental campaign, Fig.15b represents the post analysis carried on during this thesis internship. The red and black line represent the Gaussian fit and bare integration, respectively.

Fig.15 shows two examples of Cs density charts, n_k, evaluated from the raw data through an entire day of experimental campaign. Fig.15a illustrates the first analysis made when the experimental campaign was still underway, Fig.15b instead is the same analysis after improvements. On the ordinates there is the density of caesium, in m^{-3}, and on the abscissa the absolute time, given in h:min:s. As it can be seen, the charts contain "base" values of density, corresponding to vacuum phase, interrupted by high values of density, in correspondence of plasma phases. It is clear that the density evaluation was improved both during plasma phase and vacuum phase. Furthermore, the Gaussian fit and bare integration were much more aligned in terms of Cs density evaluation.

After examining all days of the campaign, a script was developed to do the following procedures, both for a specified time range and for the entire day of the experimental campaign:

- calculate mean values of Cs density both for vacuum phase and plasma phase
- identify peaks of Cs value, produced by plasma shots inside the source, within a single period of analysis
- make a report of all the values found, so as to easily access the Cs density data of each time interval or of each absorption peak.

All these procedures just described are to be considered separately executed for density values calculated from bare integration and Gaussian fit.

To be able to distinguish plasma phase from vacuum phase, the width of the peaks was examined, due to the above mentioned plasma-Cs interaction. Specifically, density values were considered coming from vacuum phase if the average width of the four peak, detected by the four LoS, was less than 1.8 pm. This value was extracted by looking at the data coming from the LoS. Furthermore, Cs density values coming from plasma phase that exceeded over 3σ from the mean values were discarded. Sometimes disturbances (e.g. mechanical vibrations or plotting errors of the program) could give spikes of density way off the density range $10^{13}\mathrm{m}^{-3}$-$10^{16}\mathrm{m}^{-3}$ mentioned in Section 2.2. The script developed was able to cut off these data automatically and therefore these values were not considered even to extract a single mean value for plasma phase.

From now on, also plasma phase and vacuum phase will be executed separately.

In order to extrapolate a mean value of density for each LoS, a linear interpolation was executed (with the `INTERPOL` function from `IDL` programming language), which computes the mean value by linearly interpolating the raw data, given in input, with the corresponding time of acquisition. It was chosen to interpolate with the LoS2 time for each of the four LoS for the reason mentioned before, i.e. LoS2 was the less disturbed LoS. Then an average of the means of the four LoS was done to extract a single values of Cs density, the measurements uncertainties considered is the standard error of the mean ($\sigma/\sqrt{N}$). A specified range of time was chosen according to the Cs flux of the ovens. In particular, the time intervals were identified on the basis of information recorded during the experimental sessions. Time intervals were identified with the Cs ovens active and with stable operating conditions. The relevant data of the ovens utilised includes: date, open and close time, Cs evaporation rate (in $\mathrm{mg\,h}^{-1}$), total evaporation time (in s) and total Cs evaporated (in mg) of the three ovens. With this information, it was distinguished between uniform and not uniform conditions in terms of Cs evaporation rate. In uniform condition the Cs rate of each oven differs from the others by less than 10%, above this threshold the ovens were considered not uniform. Fig.16 shows an example plot of the Cs density values and how the script identifies the peaks generated by the plasma. The density values just calculated come from bare integration and Gaussian fit, of about 1 hour period of Cs evaporation during uniform condition. The dotted red line represents the mean value of Cs density during plasma phase, the black one during vacuum phase and the green one represents the Gaussian mean density. The difference between the latter two values is within 9%. All the peaks, standing for plasma phases, were successfully identified.

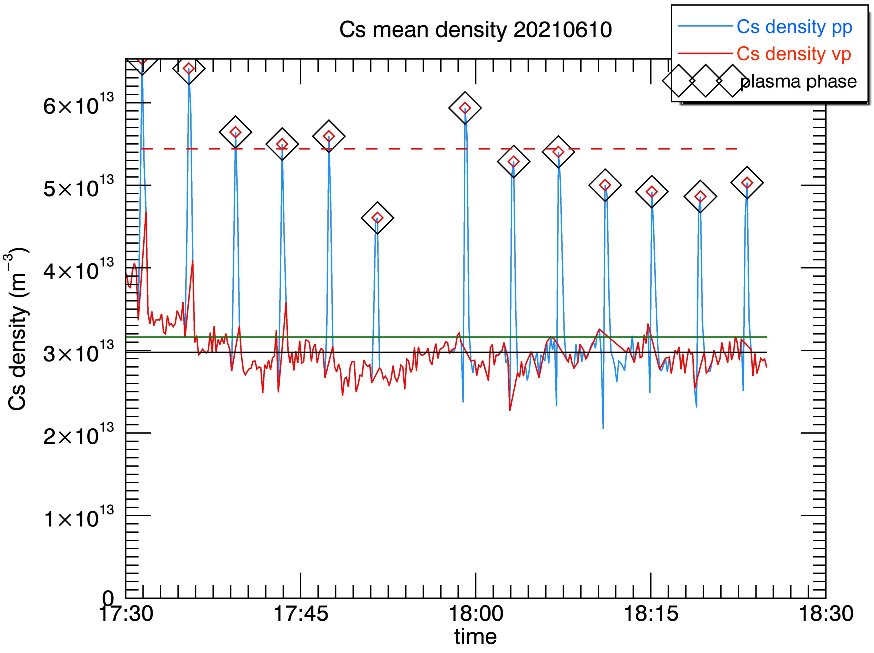

Figure 16: Cs density plot, during hydrogen operation. The red line shows the Cs density value evaluated in vacuum phase (vp), the blue line indicates the Cs density in presence of plasma (pp) and the diamond squares illustrate the identified plasma peaks.

3.2 Description of results

In order to describe the Cs spatial distribution along the PG and caesium characteristics for plasma and vacuum phases, separated analyses were made. From the plots and data described in the previous section, it has been appreciated that Cs density values obtained from bare integration of the four LoS were more stable than the ones calculated from the Gaussian fit. This section will refer only to the first ones.
Initially, in order to characterise the presence of caesium, all the Cs mean density values, with the corresponding uncertainties, coming from all the four LoS were divided in uniform and nonuniform, related to the Cs evaporation rate of the ovens, period of time and in vacuum-plasma phase. Uniform and nonuniform periods of analysis include vacuum and plasma phase, so it will be specified when the first periods are to be considered separated from the second. The correspondent sums of the three Cs evaporation rate from the ovens were associated to each uniform and not uniform period. The plot in Fig.17 shows the average Cs values as a function of the total Cs evaporation rate, in vacuum phase. The maximum average value of Cs density inside the source is essentially similar in uniform and not uniform conditions and overall grows linearly with the total caesium evaporated. Consequently, detecting stationary conditions of long intervals of Cs evaporation (in the order of an hour) does not mean that the best possible conditioning of the source has been achieved, in terms of caesium coverage.

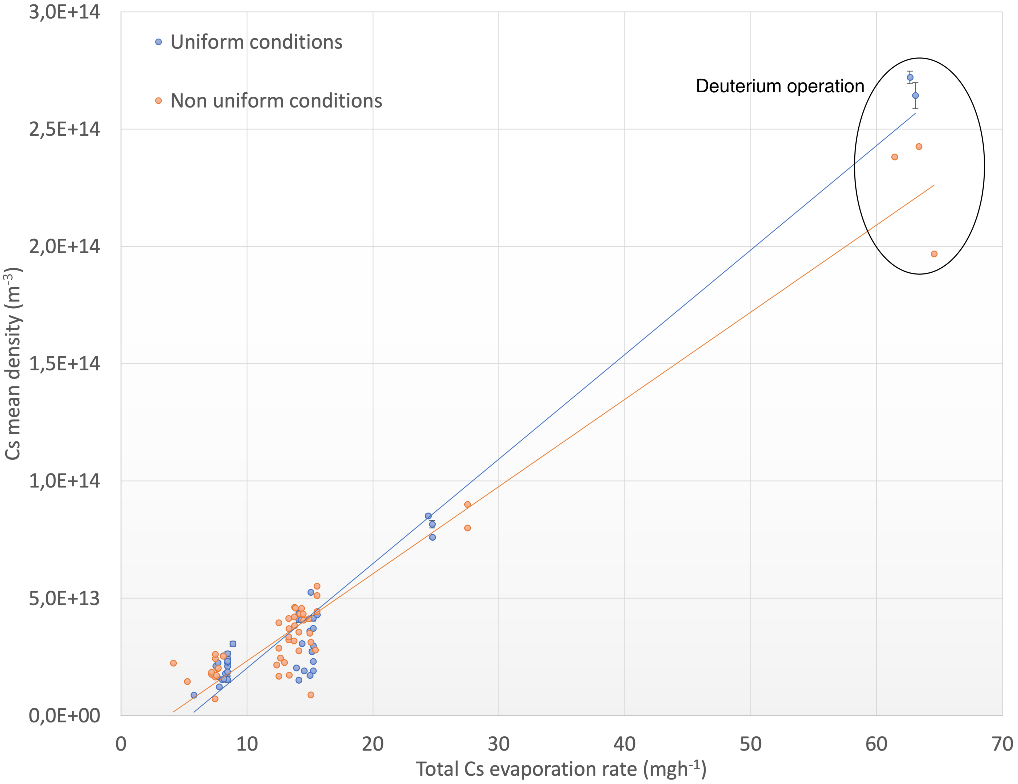

Figure 17: Average Cs density measured in vacuum phases by LAS as a function of total Cs evaporation rate from the Cs ovens. Blue and orange dots refer to uniform and non-uniform evaporation conditions, respectively.

Instead, in order to get the Cs spatial distribution, the mean Cs density values, for each LoS, were inspected as function of the evaporation rate of the ovens, strictly in uniform condition[5] and in vacuum phase. The results are shown in Fig.18.
Fig.18 illustrates that, given a fixed value of evaporation rate, in the vast majority of the case

---

[5] The spatial distribution could be otherwise influenced.

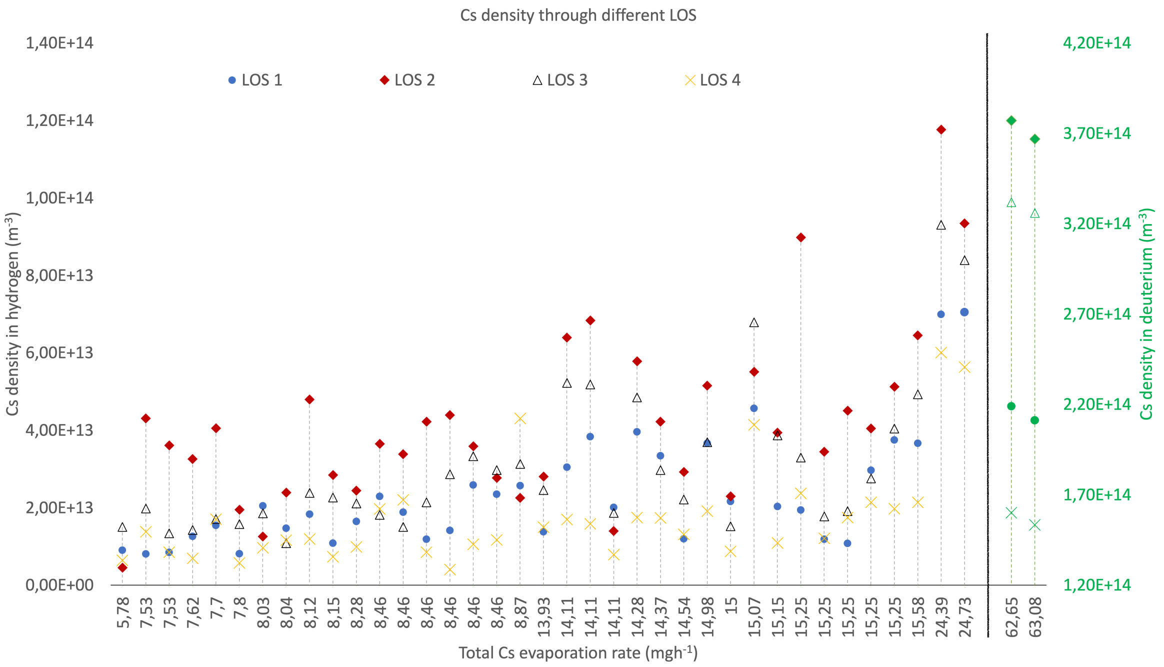

Figure 18: Cs density as measured by each LoS, under uniform evaporation conditions. The green data, on the right side of the black band, refers to the deuterium operations, whose density is indicated by the right y-axis.

LoS2 and LoS3 detect the highest Cs density values, followed by LoS1 and LoS4. This means that, when Cs is evaporated inside the source, it accumulates in the top middle section of the source along the PG. Moreover, it can be pointed out that the bottom (LoS3 and LoS4) of the source detects the least average value of Cs density due to the action of plasma, which is subject to vertical mostly upwards drifts caused by the magnetic filter field discussed in Section 1.4 [10, 26, 27].

The last two days of experimental campaign were carried out in deuterium plasma. A typical density profile evaluation is shown in Fig.19. In the presence of plasma, the Cs density profile has a spike and immediately after a remarkable drop, detecting density values which are locally lower than the ones before the same spike. Those are probably due to the fact that deuterium has twice as much mass as hydrogen and consequently the erosion of caesium from the PG is higher and there is a significant redistribution of Cs inside the source [28]. The difference between hydrogen and deuterium is clear in terms of Cs erosion, indeed in Fig.20 immediately afterwards the plasma spike the Cs values in vacuum phase soon stabilise to about the identical value before the same spike.

Moreover, the plasma has a visible effect also on the absorption lines of caesium. Fig.21 shows this effect, detected by LoS2. The peaks in the plasma phase result more broadened and higher with respect to the vacuum phase (meaning no plasma in the chamber), the plasma induces the Doppler broadening discussed in Section 2.2 and gives higher peaks on the absorption spectra.

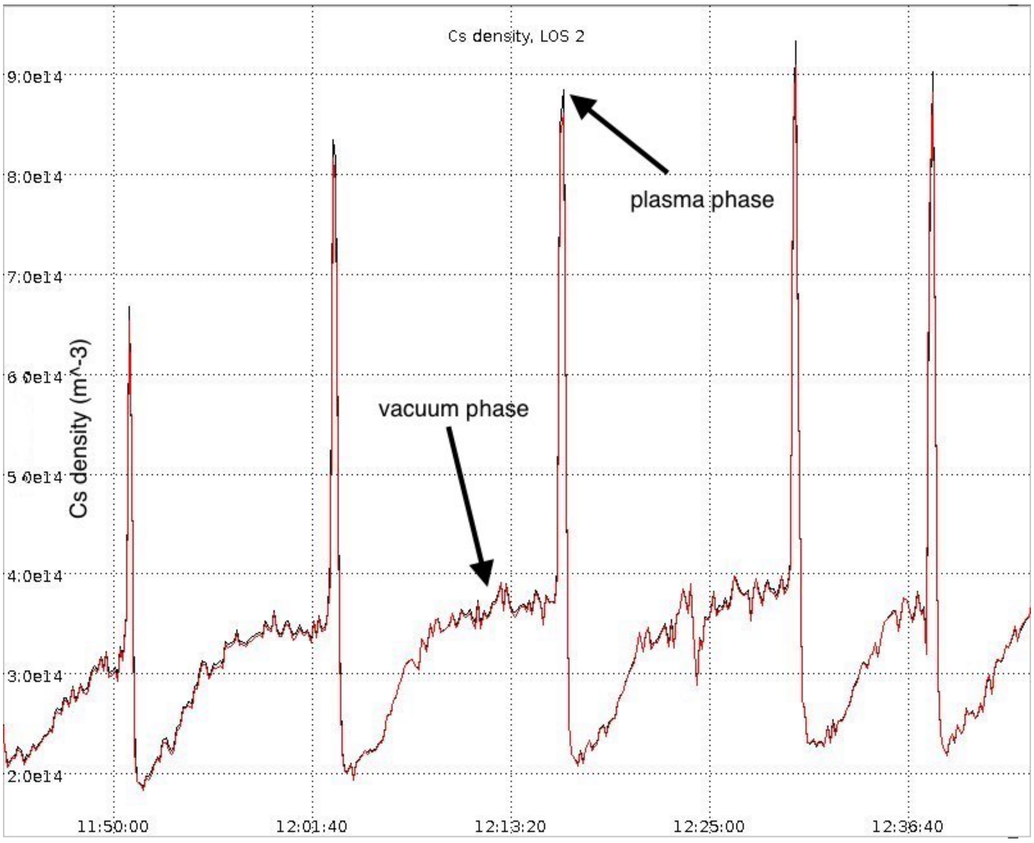

Figure 19: Cs density value in deuterium operation by seen from LoS2.

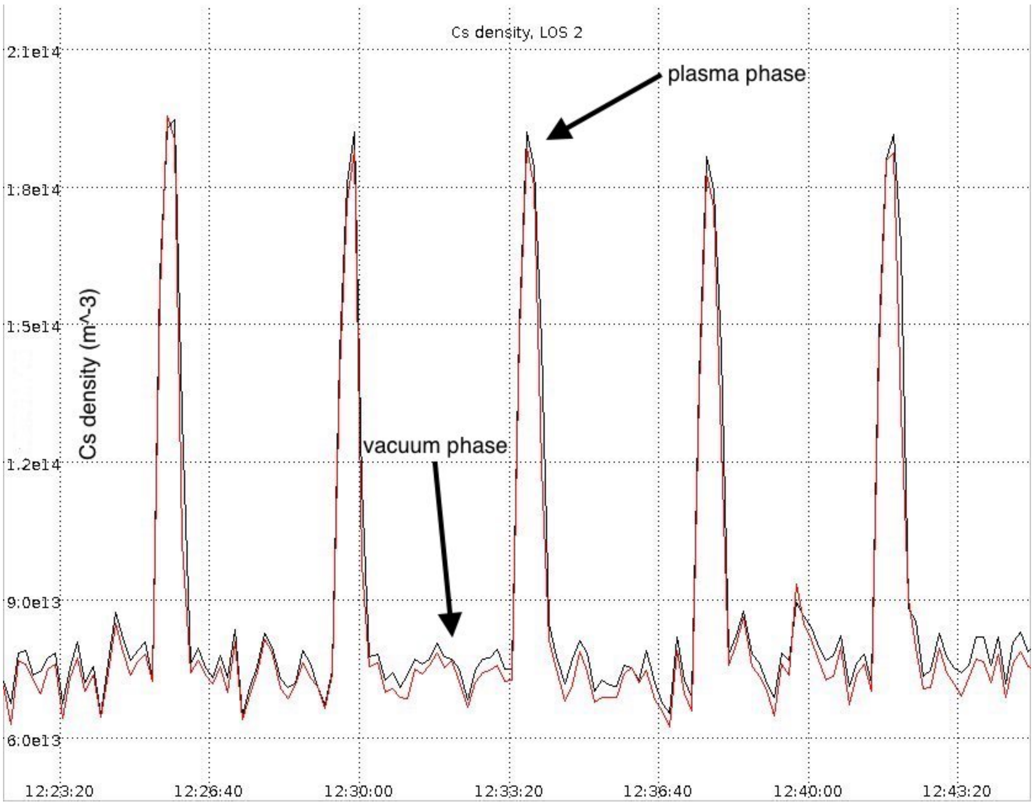

Figure 20: Cs density value in hydrogen operation by seen from LoS2.

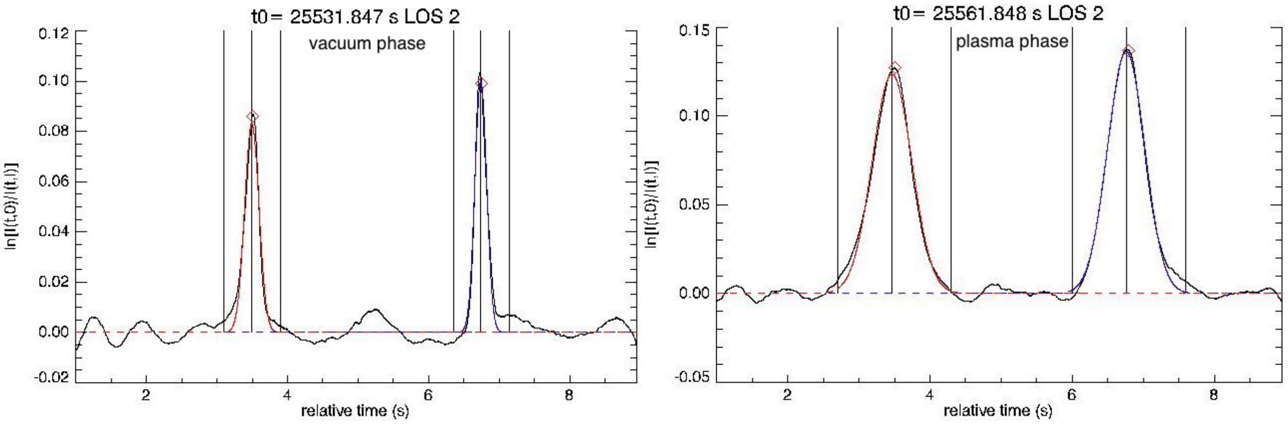

Figure 21: Plasma effect on the Cs absorption line. The picture on the left shows the logarithm of the ratio, between the intensity of the laser before and after traversing the chamber volume, in vacuum phase as a function of the time t (s). On the right instead the same quantity is shown in the presence of plasma inside the chamber.

4 Conclusion

In this thesis the caesium spatial distribution has been characterised by means of absorption spectroscopy diagnostic implemented inside SPIDER: LAS.
This diagnostic has provided useful information about the caesium distribution inside the source, along with the plasma erosion on the caesiated surface of the PG. Improvements have been made on the data analysis carried out in the 2021 campaign. Specifically, by changing parameters on the code, the analysis has been made specific for plasma phase and vacuum phase, resulting in an enhancement in data quality.

The analysis shows that caesium distribution is more accentuated at the middle-top part of the source and less at the bottom. This fact may be explained by the plasma interaction with the surfaces of the PG which wears away part of the caesium and redistributes it, according to the results showed in this thesis.
The maximum average value of Cs density inside the source is essentially similar in uniform and not uniform conditions (see Section 3.2) and overall grows linearly with the total caesium evaporated by the ovens. The operation carried out in deuterium showed that much more Cs was eroded from the PG, due to the higher mass of ^{2}H, and consequently the average Cs density values detected were higher with respect to the operation carried out in hydrogen.
Furthermore, it has been observed that plasma has a visible effect also on the absorption lines of caesium, resulting in more broadened peaks with respect to vacuum phase due to the Doppler effect.

From this thesis work, it emerges that injecting Cs inside SPIDER increments the negative ion production, but improvements may be done in order to enhance the uniformity of the extracted beams. For instance, further study on PG and BP could be done in order to reduce the coextracted electrons even more, without affecting the negative ion beams. The limitations on having only two days of operation on deuterium has not allowed to deepen the knowledge on Cs erosion. This has to be taken into account for long plasma pulses (up to 3600 s), necessary for NBI to be effective. As a matter of fact, having longer pulses means that deuterium will be more in contact with the PG surface, which will be consequently more eroded. Additional improvement could be done in the stability of the LoS inside the source, in particular for LoS1 and LoS4, which were the ones more affected by mechanical vibrations.

References

[1] "Energy Statistics Data Browser – Data Tools - IEA."

[2] International Energy Agency, *Electricity Market Report*, *Electricity Market Report* (2022) 118.

[3] "ITER - the way to new energy." https://www.iter.org/.

[4] M. Kikuchi, K. Lackner and M. Quang, *Fusion Physics*, Iaea (2012).

[5] S.M.G. de Vicente, N.A. Smith, L. El-Guebaly, S. Ciattaglia, L.D. Pace, M. Gilbert et al., *Overview on the management of radioactive waste from fusion facilities: ITER, demonstration machines and power plants*, *Nuclear Fusion* **62** (2022) 085001.

[6] M. Kikuchi and I. Nobuyuki, *Role of fusion energy for the 21 century energy market and development strategy with international thermonuclear experimental reactor*, in *https://fire.pppl.gov/energy_ja_wec01.pdf*, 2001.

[7] R.S. Hemsworth, D. Boilson, P. Blatchford, M.D. Palma, G. Chitarin, H.P.L. de Esch et al., *Overview of the design of the ITER heating neutral beam injectors*, *New Journal of Physics* **19** (2017) 025005.

[8] G. Serianni, V. Toigo, M. Bigi, M. Boldrin, G. Chitarin, S. Dal Bello et al., *SPIDER in the roadmap of the ITER neutral beams*, *Fusion Engineering and Design* **146** (2019) 2539.

[9] E. ITER, *Documentation series no. 24 iter technical basis*, *IAEA, Vienna* (2002) .

[10] E. Sartori, M. Agostini, M. Barbisan, M. Bigi, M. Boldrin, M. Brombin et al., *First operations with caesium of the negative ion source SPIDER*, *Nuclear Fusion* **62** (2022) 086022.

[11] R.G. Wilson, *Electron and Ion Emission from Polycrystalline Surfaces of Nb, Mo, Ta, W, Re, Os, and Ir in Cesium Vapor*, *Journal of Applied Physics* **37** (1966) 4125.

[12] S. Cristofaro, R. Friedl and U. Fantz, *Correlation of Cs flux and work function of a converter surface during long plasma exposure for negative ion sources in view of ITER*, *Plasma Research Express* **2** (2020) 035009.

[13] M. Barbisan, R. Agnello, G. Casati, R. Pasqualotto, C. Poggi, E. Sartori et al., *Negative ion density in the ion source SPIDER in Cs free conditions*, *Plasma Physics and Controlled Fusion* **64** (2022) 065004.

[14] L. Schiesko, P. McNeely, P. Franzen, U. Fantz and the NNBI Team, *Magnetic field dependence of the plasma properties in a negative hydrogen ion source for fusion*, *Plasma Physics and Controlled Fusion* **54** (2012) 105002.

[15] G. McKee, R. Fonck, B. Stratton, R. Bell, R. Budny, C. Bush et al., *Confined alpha distribution measurements in a deuterium-tritium tokamak plasma*, *Physical review letters* **75** (1995) 649.

[16] M. Bacal, A.M. Bruneteau, C. Deniset, L.I. Elizarov, F. Sube, A.Y. Tontegode et al., *Effect of cesium and xenon seeding in negative hydrogen ion sources*, *Review of Scientific Instruments* **71** (2000) 1082.

[17] B.E. Keen, M. Huguet, R. Hemsworth and JET Project., *Fusion technology 1990 : proceedings of the 16th Symposium on Fusion Technology, London, U.K., 3-7 September 1990. Vol. 1*, *Fusion Technology 1990* (1991) .

[18] A. Rizzolo, M. Pavei and N. Pomaro, *Caesium oven design and R&D for the SPIDER beam source*, *Fusion Engineering and Design* **88** (2013) 1007.

[19] E. Sartori, *Simulation-based quantification of alkali-metal evaporation rate and systematic errors from current–voltage characteristics of langmuir–taylor detectors*, *IEEE Transactions on Instrumentation and Measurement* **69** (2020) 4975.

[20] B. Heinemann, H. Falter, U. Fantz, P. Franzen, M. Fröschle, R. Gutser et al., *Design of the "half-size" ITER neutral beam source for the test facility ELISE*, *Fusion Engineering and Design* **84** (2009) 915.

[21] S. Cristofaro, M. Fröschle, A. Mimo, A. Rizzolo, M. De Muri, M. Barbisan et al., *Design and comparison of the Cs ovens for the test facilities ELISE and SPIDER*, *Review of Scientific Instruments* **90** (2019) 113504.

[22] M. Barbisan, R. Pasqualotto and A. Rizzolo, *Design and preliminary operation of a laser absorption diagnostic for the SPIDER RF source*, *Fusion Engineering and Design* **146** (2019) 2707.

[23] A. Kramida, Yu. Ralchenko, J. Reader and and NIST ASD Team. NIST Atomic Spectra Database (ver. 5.10), https://physics.nist.gov/asd. National Institute of Standards and Technology, Gaithersburg, MD., 2022.

[24] U. Fantz and C. Wimmer, *Optimizing the laser absorption technique for quantification of caesium densities in negative hydrogen ion sources*, *Journal of Physics D: Applied Physics* **44** (2011) 335202.

[25] M. Barbisan, S. Cristofaro, L. Zampieri, R. Pasqualotto and A. Rizzolo, *Laser absorption spectroscopy studies to characterize cs oven performances for the negative ion source SPIDER*, *Journal of Instrumentation* **14** (2019) C12011.

[26] C. Poggi, M. Spolaore, M. Brombin, R. Cavazzana, M. Fadone, R. Pasqualotto et al., *Langmuir probes as a tool to investigate plasma uniformity in a large negative ion source*, *IEEE Transactions on Plasma Science* **50** (2022) 3890.

[27] G. Serianni, E. Sartori, R. Agnello, P. Agostinetti, M. Agostini, M. Barbisan et al., *Spatially resolved diagnostics for optimization of large ion beam sources*, *Review of Scientific Instruments* **93** (2022) 081101.

[28] M. Barbisan, R. Agnello, L. Baldini, G. Casati, M. Fadone, R. Pasqualotto et al., *Characterization of cesium and H-/D- density in the negative ion source spider*, *Fusion Engineering and Design* **194** (2023) 113923.